



## Remote sensing of snow thaw at the pan-Arctic scale using the SeaWinds scatterometer

Michael A. Rawlins<sup>a,\*</sup>, Kyle C. McDonald<sup>b</sup>, Steve Frohling<sup>a,c</sup>, Richard B. Lammers<sup>a</sup>, Mark Fahnestock<sup>a</sup>, John S. Kimball<sup>d</sup>, Charles J. Vörösmarty<sup>a,c</sup>

<sup>a</sup>Water Systems Analysis Group, Institute for the Study of Earth, Oceans, and Space, University of New Hampshire, Durham, NH 03824, USA

<sup>b</sup>Jet Propulsion Laboratory, California Institute of Technology, Pasadena, California, USA

<sup>c</sup>Department of Earth Sciences, University of New Hampshire, Durham, NH 03824, USA

<sup>d</sup>School of Forestry/NTSG, The University of Montana, Missoula, Montana, USA

Received 21 January 2004; revised 30 November 2004; accepted 21 December 2004

### Abstract

Remotely sensed estimates of snow thaw offer the potential of more complete spatial coverage across remote, undersampled areas such as the terrestrial Arctic drainage basin. We compared the timing of spring thaw determined from approximately 25 km resolution daily radar backscatter data with observed daily river discharge time series and model simulated snow water content data for 52 basins (5000–10,000 km<sup>2</sup>) across Canada and Alaska for the spring of 2000. Algorithms for identifying critical thaw transitions were applied to daily backscatter time series from the SeaWinds scatterometer aboard NASA QuikSCAT, the observed discharge data, and model snow water from the pan-Arctic Water Balance Model (PWBM). Radar-derived thaw shows general agreement with discharge increases (Mean Absolute Difference, MAD=21 days,  $r=0.45$ ), with better agreement (16 days) in basins with moderate-high runoff due to snow thaw. Even better agreement is noted when comparing the scatterometer-derived primary thaw timing with model simulated snow water increase (MAD=14 days,  $r=0.75$ ). Good correspondence is found across higher latitude basins in western Canada and Alaska, while the largest discrepancies appear at the driest watersheds with lower snow and daily discharge amounts. Extending this analysis to the entire pan-Arctic drainage basin, we compared scatterometer-derived date of the primary (maximum) thaw with the timing of simulated snow water increases from the PWBM. Good agreement is found across much of the pan-Arctic; discrepancies for over half of the analyzed grid cells are less than one week. MADs are 11.7 days for the Arctic basin in Eurasian and 15.1 days across North America. Mean biases are low; 2.1 and  $-3.1$  days for Eurasia and North America, respectively. Stronger backscatter response (high signal-low noise) is noted with higher seasonal snow accumulation, low to moderate tree cover and low topographic complexity. Although our results show inconsistent performance along coastal regions and warmer southerly parts of the study domain, active radar instruments such as SeaWinds offer the potential for monitoring high-latitude snow thaw at spatial scales appropriate for pan-Arctic applications

\* Corresponding author. Tel.: +1 603 862 1053; fax: +1 603 862 0587.

E-mail address: [rawlins@eos.sr.unh.edu](mailto:rawlins@eos.sr.unh.edu) (M.A. Rawlins).

in near real time. Applications include hydrological model verification, analysis of lags between snow thaw and river response, and determination of large-scale snow extent.

© 2005 Elsevier B.V. All rights reserved.

*Keywords:* Snow; Scatterometer; SeaWinds; Runoff; Pan-Arctic

## 1. Introduction

The climate and hydrological cycle of the Arctic have undergone rapid change in recent decades (Serreze et al., 2000). Among the changes are increased winter air temperatures (Chapman and Walsh, 1993; Rawlins and Willmott, 2003; Robeson, 2004), reduced snow cover (Serreze et al., 2000), warming of permafrost (Osterkamp and Romanovsky, 1999; Romanovsky et al., 2002), increased runoff and river discharge (Peterson et al., 2002), and reduced extent of sea ice cover (Serreze et al., 2002; Rothrock et al., 2003). These significant changes are occurring over large spatial domains. The combination of remoteness and extreme climate have led to a relatively low density of ground-based hydrological and meteorological observation stations. This sparse network hinders the development of strong baseline hydrological and meteorological time series data, the ability to detect change occurring across large regions, and the search for strong explanatory relationships linking the changing components of the arctic hydroclimatic system. Satellite-borne remote sensing can provide large spatial coverage at high temporal resolution, and thus may be able to contribute to our ability to observe and understand the pan-Arctic system. The expanded use of remotely sensed data has recently been cited as a vital component in the study of Arctic environmental change (Vörösmarty et al., 2001).

Satellite-borne microwave radars provide year-round all-weather capability for monitoring high latitude ecosystems. Wide-swath coverage provided by current scatterometer instruments (~1800 km for SeaWinds at ~25 km spatial resolution) allows observations of the polar regions at sub-daily time-scales. Combined with their day/night measurement capability, and high sensitivity to the freeze/thaw state of water within the landscape, these instruments offer distinct advantages over optical and near-IR sensors for monitoring hydrologic processes across the pan-Arctic land mass.

Microwave backscatter is sensitive to structural and dielectric properties of water and vegetation in the scanned swath (Elachi, 1987). Short wavelength radar such as the current  $K_u$  band SeaWinds scatterometer (wavelength=2.2 cm; frequency=13.4 GHz) and the earlier NASA scatterometer (NSCAT; 2.1 cm; 14 GHz), can exhibit significant diffuse or volume scattering from dry snow (Raney, 1998; Ulaby and Dobson, 1986) and thus should be able to monitor seasonal snow cover at large scales (Nghiem and Tsai, 2001). At snow thaw, the ripening snow will contain a significant quantity of liquid water (with a very high dielectric constant), surface scattering will dominate the microwave interaction with the snow, and backscatter should decrease dramatically. It is likely that the lowest backscatter signals occur on days when the landscape surface element (resolution is an ellipse of roughly  $37 \times 25$  km) has near-continuous, very wet snow cover (Nghiem and Tsai, 2001).

Nghiem and Tsai (2001) compared winter 1996–1997, weekly-averaged NSCAT backscatter data, binned to 25 km resolution, to a northern hemisphere, weekly  $2^\circ$  resolution snow cover data set based on optical remote sensing data (NOAA/NESDIS, 1999), and to maps of snow-cover class (tundra, taiga, prairie, alpine, maritime, and ephemeral). They concluded that  $K_u$ -band backscatter was insensitive to vegetation cover across the taiga/tundra zone, and that backscatter dropped rapidly at snow thaw, as inferred both from hemispheric snow-cover and from weather station data from three sites in Alaska, three sites in Canada, and five sites in Siberia.

Wismann (2000a) examined 8 years of ERS scatterometer (C-band; 5.3 GHz; 5.5 cm) data for a spring thaw signal in Siberia. Data were averaged to 3-days, and the spatial resolution was approximately  $50 \times 50$  km. The thaw detection algorithm used an intermediate threshold based on local mean backscatter for winter and summer. He found that the onset of thaw varied locally by about one month over 1992–1999, that it took about 4 months for the thaw

signal to move from the southern part of the study region (50°N) to the northern part (75°N), and that onset of thaw correlated well with the geographical variability of air temperature. Wismann (2000b) also studied the Greenland snow thaw signal with ERS scatterometer data over this same period. Thaw detection was based on a backscatter offset of 3 dB from a winter (November–March) mean, corresponding to a 7 cm layer of snow having an 0.5% liquid water content, based on a modeling analysis by Winebrenner et al. (1994). He found a strong correlation between annually integrated positive air temperature and an annually integrated backscatter offset. In the 1992–1999 ERS scatterometer record, Wismann (2000b) found a 3-fold range in the thaw extent on Greenland.

Hillard et al. (2003) compared spatial patterns of spring thaw signals from NSCAT (active between 15 September 1996 and 29 June 1997) with simulated snow surface temperature and liquid water content from the Variable Infiltration Capacity (VIC) hydrological model (Liang et al., 1994), driven by station meteorological data (maximum and minimum air temperature and precipitation) at daily time resolution for the Upper Mississippi Basin and the BOREAS study region in central Canada. They found that only occasionally was there a similar spatial pattern in their maps of simulated snow liquid water content and scatterometer backscatter. They attributed this lack of correlation to time of day of NSCAT overpass (10:00 am and 10:00 pm, not optimal times for maximum and minimum snow liquid water content), interference from vegetation cover, and signal noise. However, their approach did not employ temporal change detection schemes to classify freeze-thaw events. Such schemes have been shown to provide effective detection of springtime thaw onset and subsequent thaw-freeze cycles when applied to active and passive microwave remote sensing data (Kimball et al., 2004a; 2004b; McDonald et al., 2004). Using scatterometer estimated freeze-thaw as an additional driver for the VIC model improved simulations only slightly in the Upper Mississippi Basin, which has a high-density network of meteorological stations providing daily driving data for the model, allowing little opportunity for improvement utilizing the 25 km resolution scatterometer data.

Kimball et al. (2004a) developed a temporal change detection algorithm for identifying springtime thaw across a 1-million km<sup>2</sup> region in central Canada, using daily scatterometer backscatter data from the earlier NSCAT instrument. During spring (defined as 1 March–31 May in their analysis), initial and final thaw dates were identified as the first and last days when the daily mean backscatter was 2.9 dB below the average backscatter of the five previous days. They also defined a day of primary thaw as the day with the lowest (i.e. most negative) daily backscatter difference of the spring period. These thaw dates were compared to daily meteorological data from 31 field stations, and were within 1 day of mean daily air temperature transitions from frozen ( $T_{\text{avg}} \leq 0$  °C) to non-frozen ( $T_{\text{avg}} > 0$  °C) conditions 97% of the time for initial and primary thaw, and 84% of the time for final thaw.

Kimball et al. (2004b) used a similar algorithm with 2000 and 2001 SeaWinds data to determine the timing and length of growing season across a North American latitudinal transect of boreal and subalpine evergreen forest stands. In this case, minimum radar backscatter thresholds were first determined as the absolute value of twice the standard deviation of daily radar backscatter differences from a moving window average of the previous 5-day period during fall (1 September–30 November) and spring (1 March–31 May). For each study site, significant positive and negative daily radar backscatter differences were identified as those exceeding prescribed thresholds. They then identified the date of the final significant backscatter difference in spring as a surrogate for the date of growing season initiation, and the date of the initial significant backscatter difference in fall as a surrogate for the date of growing season cessation. Site growing season initiation and cessation were determined from site measurements of the first and last days of the calendar year when the evergreen trees show significant trunk (xylem) sap flow and canopy net daily CO<sub>2</sub> uptake. Scatterometer-derived dates and independent ground measurements of growing season onset and length were correlated, with a mean difference of about  $\pm 5$  days.

In this study we compare the timing of spring 2000 snow thaw determined from the SeaWinds backscatter

data with daily discharge observations across 52 small (5000–10,000 km<sup>2</sup>) basins in Canada and Alaska. Our analysis then expands to the entire pan-Arctic drainage basin, where we compare the scatterometer-derived thaw timing with timing of daily simulated snow water content from the pan-Arctic Water Balance Model (PWBM) (Rawlins et al., 2003). Landscape and climatic factors that influence the radar backscatter temporal response and the agreement in thaw timing between the remotely sensed (scatterometer), observed (discharge), and modeled (PWBM snow content) data are explored. SeaWinds scatterometer data are evaluated here to better understand the potential benefits as well as the limitations of using microwave scatterometer data in the study of high-latitude hydrology.

## 2. Data sources and methods

Timing of snow thaw is derived from daily SeaWinds backscatter time series, daily river discharge data, and model simulated daily snow water content during spring of 2000. The spatial data is gridded to a 25×25 km Lambert Azimuthal equal area EASE-Grid (NSIDC, 1995; Brodzik and Knowles, 2002). Our large-scale analysis encompasses the pan-Arctic drainage basin, which extends as far south as 45°N in southern Canada and southern Siberia (Fig. 1). Given a lack of seasonal snow thaw, regions of permanent ice are excluded from our analysis. Areas with insufficient model snow water (described below) are also eliminated. The resulting

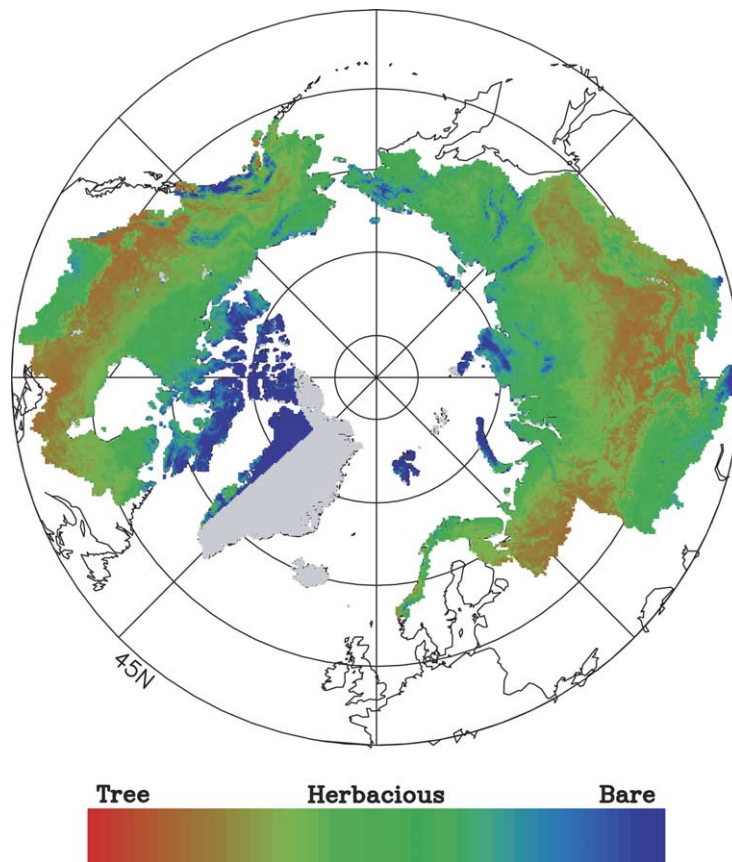


Fig. 1. Moderate Resolution Imaging Spectroradiometer (MODIS)-derived vegetation cover (Hansen et al., 2003) across the pan-Arctic drainage basin. Colored regions show land areas which drain northward to the Arctic Ocean. MODIS cover fractions of tree, herbaceous, and bare ground sum to 100% and are shown following aggregation to the 25 km EASE-Grid. Each grid is colored with red, green, and blue intensities representing fractions of tree, herbaceous, and bare ground, respectively. Circles locate the 52 study basins (5000–10,000 km<sup>2</sup>) with observed daily hydrographic data used in this study. Grids with missing MODIS data are shaded in gray.

32,896 grid points ( $\sim 21$  million  $\text{km}^2$ ) are used to compare the estimates of snow thaw timing for 2000. To compare timing of thaw from the radar, river discharge, and model snowwater data, we identify a year-day (DOY) in each time series that marks the exceedence of a critical threshold indicative of thaw and/or subsequent runoff.

### 2.1. Radar backscatter

The SeaWinds scatterometer was launched onboard the QuikSCAT satellite on June 19, 1999 as a follow-on instrument to the NSCAT sensor, and continues to operate into 2004. The SeaWinds instrument consists of a rotating, pencil-beam antenna, which provides contiguous measurement swaths of 1400 km (inner-beam) and 1800 km (outer-beam), coverage of approximately 70% of the Earth on a daily basis and 90% global coverage every 2 days. Overlapping orbit tracks at higher latitudes improve SeaWinds temporal coverage, providing multiple backscatter measurements each day for much of the pan-Arctic land mass. We are thus able to partition the daily measurements by ascending and descending node tracks, while maintaining daily observations for each node. Ascending node data correspond to early morning observations ( $\sim 6:00$  am equator crossing time) and descending node data correspond to late-day observations ( $\sim 6:00$  pm equator crossing time). The instrument has mean incidence angles of  $54^\circ$  (outer-beam) and  $46^\circ$  (inner-beam) and a spatial resolution ranging from approximately  $37 \times 25$ -km ('egg' data) to  $6 \times 25$ -km ('slice' data). The SeaWinds scatterometer transmits at a frequency of 13.4 GHz (2.1 cm wavelength). Surface backscatter measurements have a 0.25 dB relative accuracy (King and Greenstone, 1999). In addition to landscape factors, backscatter from active radar systems is strongly affected by the dielectric properties of a snow (Elachi, 1987). High microwave frequencies (i.e. shorter microwave wavelengths) are best suited for observing snow processes owing to the increased scattering albedo for snow observed at these wavelengths (e.g. Ulaby and Dobson, 1986; Raney, 1998). As water transitions from a solid to a liquid phase, its dielectric properties change significantly (Kraszewski, 1996), giving rise to a dynamic response in the surface backscatter as the snow thaws, though

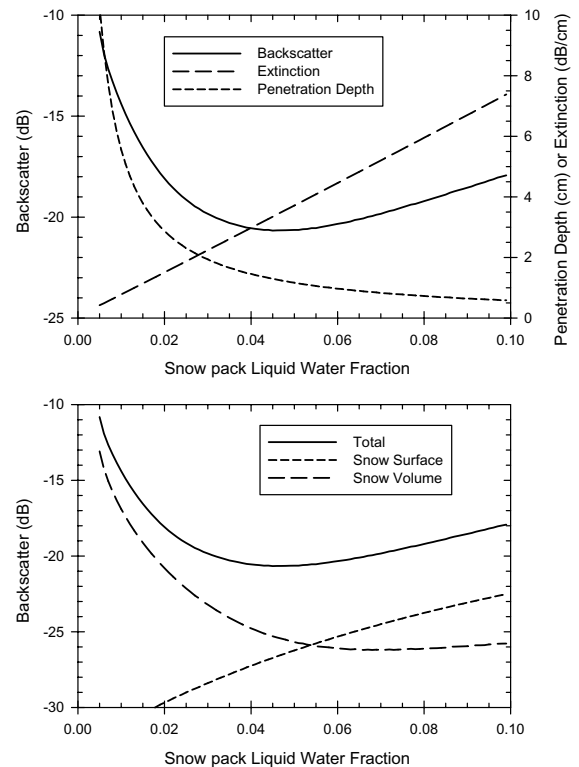


Fig. 2. Behavior of Ku-band radar backscatter with increasing snow wetness derived using a radiative transfer radar backscatter model for a wet snow (Shi and Dozier, 1995). The model was applied at Ku-band and an incidence angle of  $54^\circ$ , corresponding to the parameters of the QuikSCAT data applied in this study. We show VV-polarized backscatter for tundra snow. The top chart illustrates increasing radar extinction and a corresponding decrease in radar penetration into the snow as the amount of liquid water in the snow increases. This gives rise to a pronounced decrease in backscatter for wet snow relative to drier snow. The bottom chart shows the two dominant contributions to the total snow backscatter for wet snow, namely the backscatter from the snow surface and the volume scatter from within the snow itself. As wetness increases, the contribution of the volume backscatter diminishes while the surface scattering contribution becomes more pronounced.

the magnitude of the backscatter response is dependent on sensor wavelength, polarization and surface heterogeneity (Ulaby et al., 1989; Waring et al., 1995). At Ku-band, the effect of snow cover on backscatter is significant (Nghiem and Tsai, 2001). Fig. 2 illustrates the response of Ku-band radar backscatter to increasing snow wetness as predicted with a radar backscatter model applied to a pure, wet snow (Shi and Dozier, 1995). For illustrative

purposes, this theoretical snow was assigned properties of the type found in tundra landscapes (Sturm et al., 1995). For dry snow, extinction of the radar energy is small. Increases in the fractional content of liquid water in the snow result in increasing extinction, and a corresponding decrease in the radar signal penetration. This leads to a diminishing contribution of diffuse (volume) scatter to the total backscatter signal, and an increase in the scattering from the snow surface. At Ku-band, backscatter thus exhibits a marked decrease with the thaw onset. This effect is readily apparent for snow-covered tundra with little or no exposed vegetation. The magnitude of this decrease will diminish in more complex, heterogeneous landscapes where other landscape constituents affect the backscatter.

Snow thaw at each EASE-Grid cell is determined by an algorithm which identifies the temporal backscatter response in reference to background frozen conditions. Although the backscatter signal is affected by water phase transitions over the entire landscape surface element (snowcover, lakes, glaciers), we refer to the process as ‘snow thaw’, as lakes and glaciers make up a small fraction in each scan swath. Snow thaw events are characterized by significant daily departures (negative) from a 30-day running mean backscatter. We identify the timing of thaw based on the time-series daily ascending node data utilizing a moving window classifier. For each EASE-Grid cell, a 5-day moving window is then applied to the daily ascending node measurements to produce a running 5-day mean backscatter. To determine critical thaw events, each daily value is compared to the previous 5-day mean. We define the primary thaw date ( $t_p$ ) as the day between DOY 60 and 182 for which the decrease in daily backscatter from the 5-day mean is a maximum. More explicitly, we define the threshold

$$\delta = \overline{\sigma_5^0}(t - 5 \leq t_0 \leq t - 1) - \sigma^0(t) \quad (1)$$

where  $\overline{\sigma_5^0}(t - 5 \leq t_0 \leq t - 1)$  is the 5 day mean ascending node backscatter computed over the 5 day moving window preceding day ( $t$ ), and  $\sigma^0(t)$  is the ascending node backscatter for day  $t$  immediately following the 5-day window. The primary thaw day ( $t_p$ ) corresponds to the day  $60 \leq t \leq 182$  where  $\delta$  is a maximum. This thaw

detection algorithm is used to define  $t_p$  for year 2000 across all EASE-Grid cells defining the pan-Arctic drainage basin. Since river discharge is an integration of physical processes across a given watershed,  $t_p$  for each of the 52 basins is taken as the average of all EASE-Grid  $t_p$  within the basin. Basin extent is determined from a digital river network developed specifically for high latitude research.

## 2.2. Hydrological data

Observed daily river discharges for year 2000 are a subset of daily and monthly records for the Arctic (Lammers et al., 2001; Shiklomanov et al., 2002). Basins with a drainage area between 5000 and 10,000 km<sup>2</sup>, were selected, since delays in thawed snow water reaching the gage at the basin outlet are known to occur in relatively larger basins. A total of 55 basin represented in R-ArcticNET have daily discharge records in 2000; all are in North America. Of these, three were removed from our analysis; one due to discrepancies in gage metadata for basin characteristics and two due to the known presence of impoundments. Each basin is defined by 8–16 EASE-Grid cells.

At high latitudes, thawing of the winter snow contributes the majority of freshwater input to river systems and, eventually, the Arctic Ocean (Kane, 1997; Shiklomanov et al., 2000). As with the SeaWinds backscatter data, a thresholding scheme was employed to identify a snow thaw signal in the daily discharge data; i.e. the time of significant change in the discharge ( $Q$ ) time series. For each of the 52 study basins, the day of year in 2000 marking the snow thaw discharge pulse ( $t_Q$ ) is the day when  $Q$  reaches a critical threshold  $Q'$ ,

$$Q' = [(Q_{\max} - \bar{Q}) \times \omega_Q] + \bar{Q} \quad (2)$$

where  $Q_{\max}$  is the maximum daily discharge rate during January–June ( $\text{m}^3 \text{s}^{-1}$ ),  $\bar{Q}$  is January–February average daily discharge rate ( $\text{m}^3 \text{s}^{-1}$ ), and  $\omega_Q$  is the fraction defining a critical exceedence (unitless). This algorithm is constrained to identify the critical exceedence following the seasonal (January–June) discharge minimum. For ten study basins with zero or missing discharge during January–February,  $\bar{Q}$  becomes the average

March  $Q$ . We chose  $\omega_Q=0.1$  to determine  $t_Q$  in this study. This thaw detection algorithm is not calibrated to the respective basin discharge. Rather, the algorithms for determining SeaWinds-based snow thaw (Eq. (1)) and basin discharge increase (Eq. (2)) were independently chosen based on our understanding of the processes controlling backscatter temporal response and subsequent discharge increase.

Observed daily discharge data provide a key measure of spring thaw timing to evaluate the SeaWinds backscatter. Daily discharge data, however, are available for only a fraction of the pan-Arctic basin. Therefore we use snow liquid water content from the pan-Arctic Water Balance Model (PWBM) (Rawlins et al., 2003). The PWBM is driven by climate time series (precipitation and air temperature) from the National Center for Environmental Prediction (NCEP) reanalysis project (Kalnay et al., 1996; Uppsala et al., 2000), along with gridded fields of plant rooting depth (Vörösmarty et al., 1989) and soil characteristics of texture (Food and Agriculture Organization/UNESCO, 1995) and organic content (Global Soil Data Task, 2000). The NCEP/NCAR Reanalysis (NNR) Project is an effort to reanalyze historical data using state-of-the-art models. Reanalysis provides a modern depiction of the atmospheric hydrological budget using the Medium Range Forecasting (MRF) spectral model and the operational NCEP spectral statistical interpolation (SSI, Parish and Derber, 1992). Input and output data sets, like the scatterometer data, are gridded on the 25 km EASE-Grid across the pan-Arctic basin, and the model is run at an explicit daily time step for the year 2000. Estimates of PWBM winter 1999–2000 snowfall are determined using air temperatures from NCEP and rescaled NNR precipitation products. Six-hourly NNR precipitation forecasts (at  $2^\circ \times 2^\circ$  resolution) are aggregated to daily means and interpolated to the 25 km resolution EASE-Grid using a statistical downscaling approach based on a probability transformation (Serreze et al., 2003). Precipitation occurring on days with a mean surface air temperature of  $\leq -1^\circ\text{C}$  is considered snow and is accumulated from October through May to estimate total winter snowfall as snow water equivalent (SWE, mm). PWBM snow thaw is driven by NNR air temperature in a simple temperature index method (Willmott et al., 1985). From the snow liquid water

content we define date of snowwater initiation ( $t_M$ ) as the DOY when snow water is greater than zero for three consecutive days.

### 2.3. Land surface data

Continuous fields of land cover fraction from the Moderate Resolution Imaging Spectroradiometer (MODIS) 0.5 km vegetation continuous field data set (Hansen et al., 2003) were aggregated to the pan-Arctic EASE-Grid. The MODIS land cover data set is an annual representation of tree, herbaceous, and bare ground cover for the period November 2000 to November 2001. Continuous fields of vegetation fraction offer better representation than discrete classifications in areas of high spatial heterogeneity. The three cover fractions sum to 100%, and the 0.5 km MODIS grid cells were aggregated to the EASE-Grid (Fig. 1) using spatial averaging. Given a high degree of uncertainty in the backscatter temporal response across ice, a data set which depicts the distribution and properties of permafrost and ground ice in the Northern Hemisphere (Brown et al., 1998) is used to mask these regions from our statistical analysis. Elevation and elevation standard deviation estimates are scaled to the EASE-Grid from the GTOPO30 data set (Gesch et al., 1999; USGS EROS Data Center, 1996). High variations in regional elevation or ‘topographic complexity’ is determined by calculating the standard deviation of 5 min GTOPO30 digital elevation model (DEM) elevations within each EASE-Grid cell.

## 3. Comparison of SeaWinds-derived thaw timing and hydrological response

Methods described in Section 2 were used to estimate timing of snow thaw inferred from the SeaWinds scatterometer ( $t_P$ ), observed discharge ( $t_Q$ ), and PWBM simulated snow liquid water content ( $t_M$ ) for each of the 52 study basins. River discharge is converted to a basin-averaged runoff depth (per unit area) by dividing a basin’s discharge by the basin area (Lammers et al., 2001). Across the Kuparuk basin (Fig. 3a), a stable early season backscatter signal precedes a large signal decrease ( $\sim 8$  dB) during snow

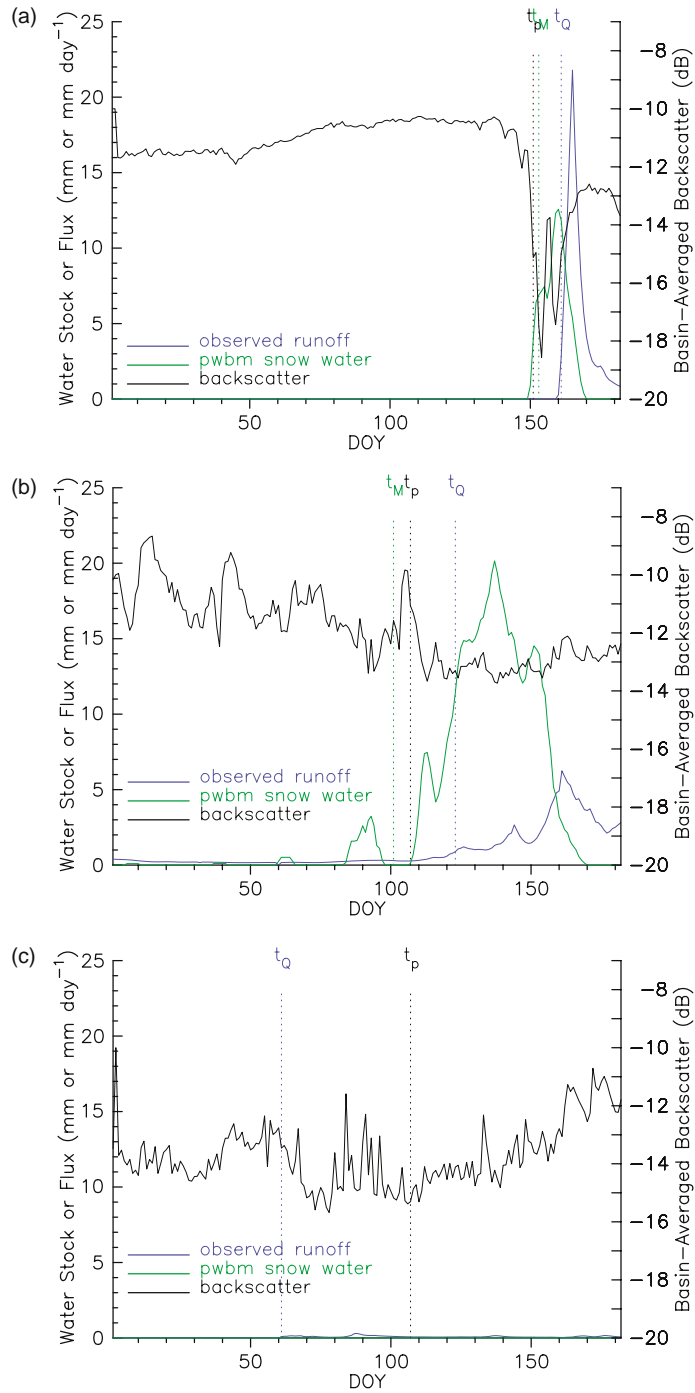


Fig. 3. Observed basin-average runoff, model snow water content, and daily SeaWinds backscatter for three of the 52 study basins, the Kuparuk (a), Murray (b), and Whitemud (c) basins. Dotted vertical lines mark dates of snow thaw-driven discharge increase ( $t_Q$ ), model snow water initiation ( $t_M$ ), and scatterometer-derived primary thaw ( $t_p$ ); see text for definitions.

thaw. PWBM snow water increase is well timed with the scatterometer response. Observed runoff increases soon thereafter. As opposed to the stable winter and large signal decrease seen across the Kuparuk, the Murray basin (mountainous, forested) experienced several backscatter decreases near DOY 50 (mid February), 62 (early March), 80–90 (late March), and DOY ~ 110 (mid April) (Fig. 3b). Model snow water increases are noted for the latter three events, resulting in a basin average  $t_M = \text{DOY } 101$ . Although the time series is quite dissimilar from the backscatter signal across the Kuparuk, basin-average values for  $t_P$  and  $t_M$  are nearly coincident. Observed basin runoff lags snow thaw in this region by ~ 10 days. The Whitemud basin in southern Manitoba, Canada experienced low snowfall and runoff during the first half of 2000 (Fig. 3c). Snow water initiation date ( $t_M$ ) is undefined across this basin, as relatively shallow snowcover is lost primarily through sublimation, with little or no simulated snow liquid water content. The backscatter signal lacks a stable winter signature and strong response during thaw which is noted in regions with continuous, ample snowcover (e.g. Kuparuk River basin, Fig. 3a). Although the signal response is fairly confused, possible thaw events near days 65 and 90 are reflected in both the SeaWinds backscatter and observed runoff. Across the Kuparuk, Murray, and, to some extent, the Whitemud basin, decreases in backscatter correlate with the PWBM snow water content, which is strongly influenced by the simulated air temperatures. This agrees with the results of Wismann (2000a) who found that the onset of scatterometer-derived thaw was correlated with air temperature and snow cover.

Our analysis here focuses on timing of scatterometer-derived primary thaw and basin runoff increase across a wide range of North American climate and landscape zones. This comparison is based on the assumption that thaw observed by the SeaWinds scatterometer has an effect on the local streamflow measured by the discharge gage. In order to represent an amount of discharge attributed to snow thaw, a snow runoff index (*snowRO*) is defined  $\text{snowRO} = RO_S - 3RO_W$ , where  $RO_S$  is total basin-average runoff from January–June and  $RO_W$  is total January–February runoff, all in millimeter for a given river basin. A large positive value of *snowRO* indicates proportionally more of the basin's river

discharge occurs after February and therefore is more likely to be the result of snow thaw. Abundant snow is an important factor in the backscatter response, since the lowest backscatter values are likely to occur when the basin has an extensive, wet snow. Thin or inhomogeneous snow will compromise the determination of thaw timing. In addition, discharge increases are not always dominated by snow thaw processes. Across the 52 study basins, correspondence between  $t_P$  and  $t_Q$  is best for later thawing basins (Fig. 4a). Across the 52 basins, the mean absolute difference ( $\text{MAD} = \frac{1}{52} \sum_{i=1}^{52} |t_Q - t_P|$ ) is 21.5 days ( $r = 0.45$ ). The mean bias ( $\text{MB} = \frac{1}{52} \sum_{i=1}^{52} t_Q - t_P$ ) is 6.1 days. Poorer agreement is evident for the basins where discharge increase occurs earliest ( $t_Q < 73$ ). Agreement between  $t_P$  and  $t_M$  ( $\text{MAD} = 14.1$  days,  $r = 0.75$ ) is comparable to the  $t_P$ ,  $t_Q$  relationship. *MB* for the  $t_P$  and  $t_M$  comparison is only  $-2.2$  days. Sensitivity to the choice of  $\omega_Q$  is not substantial. Defining  $\omega_Q = 0.1$  results in  $r = 0.50$  and  $\text{MAD} = 19.2$  days. For  $\omega_Q = 0.15$ ,  $r = 0.41$  and  $\text{MAD} = 24$  days. Discrepancies are lower across basins with moderate-high *snowRO* index (Fig. 4b). The discrepancy or difference between the two dates is largely a result of lags in snow thaw at the soil surface reaching the river system. Although the study basin sizes have been minimized to eliminate longer travel times, a bias between snow thaw and observed discharge increase is expected. Lags such as damming of snow thaw runoff has been shown to cause delays in streamflow increases during spring at high latitudes (e.g. Hinzman and Kane, 1991). Since  $t_P$  and  $t_M$  are determined for the same process, the bias ( $-2.1$  days) is lower. Considerable discrepancies are found for the basins with the lower *snowRO* index. These larger discrepancies may result from errors in the scatterometer snow thaw identification as well as deficiencies in the discharge algorithm for the driest basins. For example, the thresholding scheme to identify  $t_Q$  (Eq. (2)) is unable to capture discharge/runoff increases across the basins with variable winter flow and small increases during spring. Large negative discrepancies occur predominately across the basins with lower tree cover (Fig. 4c), many of which are drier prairie basins with low *snowRO* (open circles in Fig. 4c). Good agreement is noted for moderate (20–50%) tree cover, with the largest positive discrepancies for basins with highest tree cover.

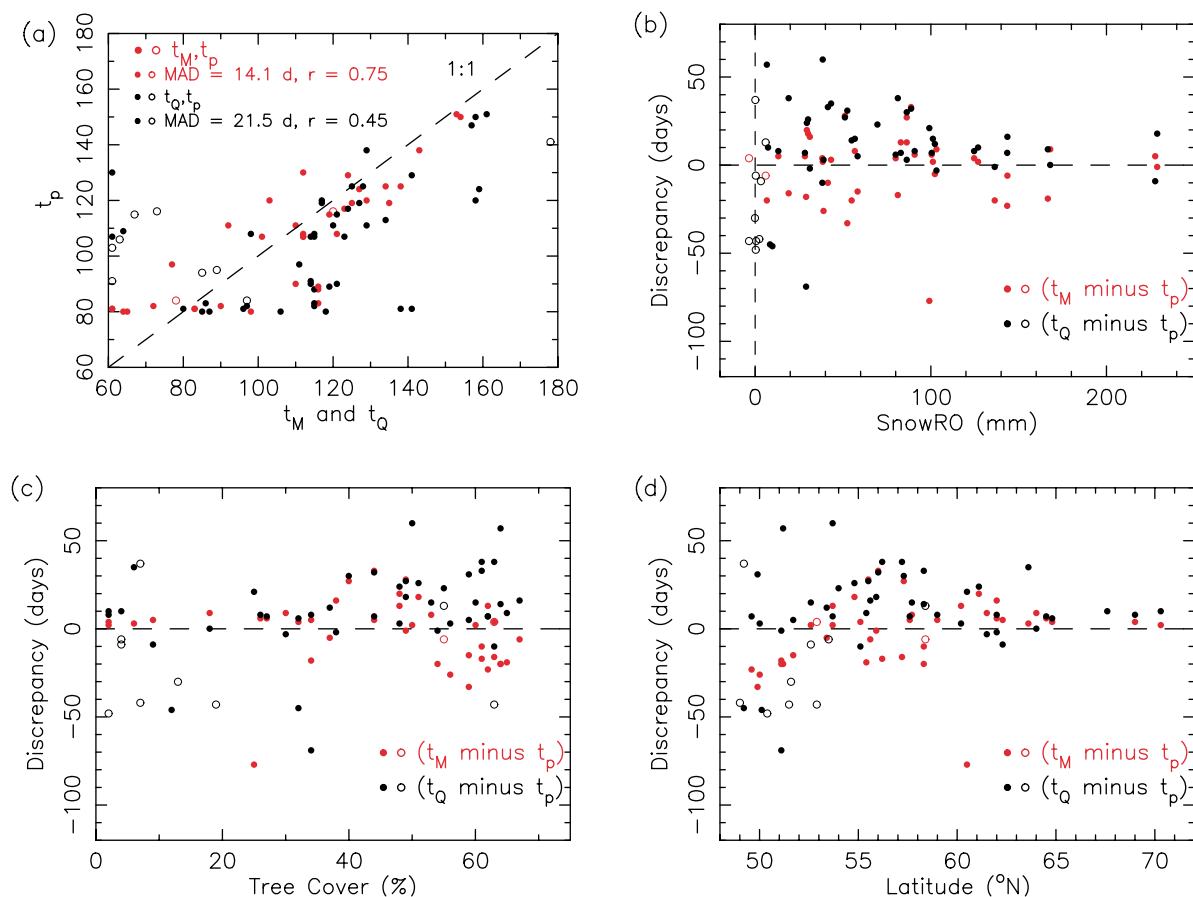


Fig. 4. Comparison of hydrological event dates ( $t_Q$ ,  $t_M$ ) and scatterometer-derived thaw date ( $t_p$ ) for the 52 study basins with observed discharge data. Comparisons between  $t_Q$  and  $t_p$  are in black.  $t_p$  vs.  $t_M$  relations are shown in red. Open circles in (a–d) identify the 10 basins with the lowest snow thaw runoff values. Discrepancies ( $t_Q - T_p$ ,  $t_M - T_p$ ) are expressed as a function of snow thaw-driven runoff (b), MODIS fractional tree cover (c), and latitude (d). Lowest discrepancies generally occur at higher latitudes, areas with high snow thaw runoff amounts and moderate tree cover. Higher discrepancies for the driest basins are attributable to limitations in both the remotely sensed data and our simple indexing methodology (Eqs. (1) and (2)).

Higher latitude sites have lower discrepancies (Fig. 4d). This is intuitively expected, as high latitude basins with frozen soils during thaw season have a lower soil infiltration capacity, causing a quicker streamflow response following snow thaw.

#### 4. Comparison of snow thaw timing across the pan-arctic domain

Given a lack of observed daily discharge data across much of the pan-Arctic drainage basin, we make use of the relatively good correspondence

between scattermeter thaw timing ( $t_p$ ) and timing from the PWBM snow water content ( $t_M$ )—determined across the 52 study basins with observed discharge—to examine the spatial pattern of the pan-Arctic discrepancies ( $t_M - t_p$ ). Across the pan-Arctic basin, a spatially-coherent pattern in  $t_p$  is evident (Fig. 5). Areas of permanent ice (shown in gray) are excluded from the large-scale statistical analysis. Across Canada, a noticeable gradient exists where the boreal forest transitions to high-latitude tundra. Across the prairies,  $t_p \geq 160$  are suspiciously late. Snow thaw occurs earliest in the boreal forest ( $t_p \sim 80$ ) in Canada and western Eurasia, while thaw progresses

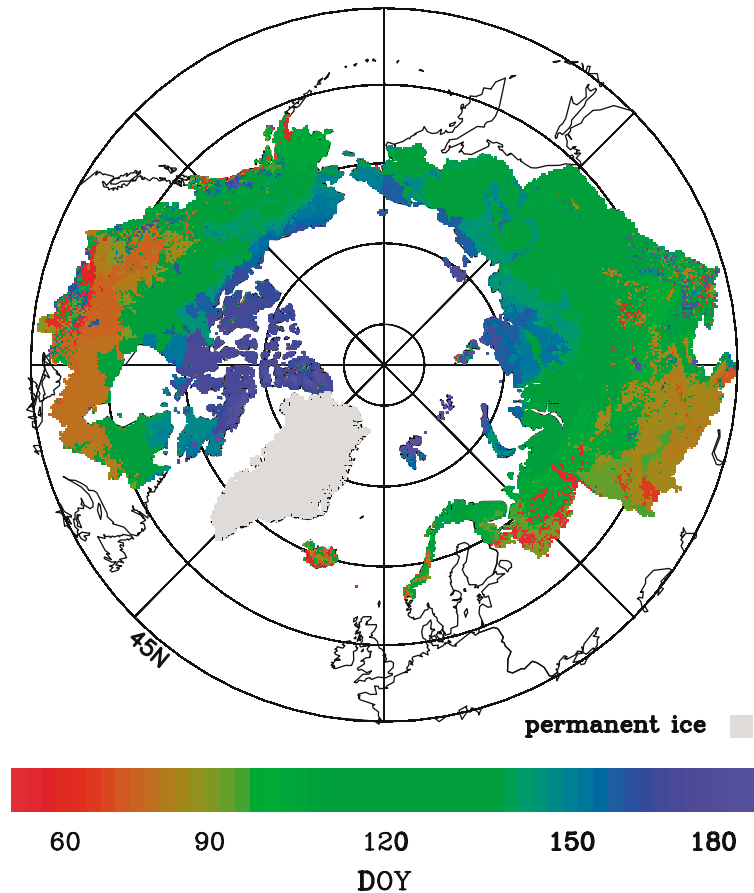


Fig. 5. Primary thaw date ( $t_p$ ) derived from the SeaWinds scatterometer for year 2000. A moving window algorithm is used to determine timing of final thaw from SeaWinds ascending pass data at each EASE-Grid cell of the pan-Arctic drainage basin (see text for details). Grid cells across Greenland and other areas of permanent ice are masked in gray due to the limited presence of snow thaw.

in a general south to north pattern across the entire pan-Arctic. High elevations in eastern Asia are well resolved, with thaw occurring 7–10 days later than the surrounding lowlands. High spatial variations are noted in the boreal forest and mountainous areas in central Eurasia. The spatial pattern in  $t_M$  (Fig. 6) is, in general, similar to the pattern in  $t_p$ . In addition to regions of permanent ice, areas lacking three consecutive days of PWBM snow water (shaded in yellow) are eliminated from the statistical analysis. In contrast to  $t_p$  patterns, the  $t_M$  field is more smooth, lacking the high spatial variations (speckled pattern) across much of the Arctic. This result is attributable to coarse NNR climate inputs (derived from sparse weather stations) driving the PWBM model. High spatial variations in  $t_p$  across central Eurasia arise

from the effects of tree cover and elevation variations on the backscatter response. Along coastal sections,  $t_M$  tends to occur early due to the wet maritime climate and frequent early spring freeze/thaw conditions. Best agreement between  $t_M$  and  $t_p$  is found across the tundra of central and northwestern North America, eastern Russia, and eastern Siberia (Fig. 7). Large negative discrepancies dominate the coastal locations-southern Alaska, across Iceland and Norway. Across the pan-Arctic basin, 49.4% of the grid cells have discrepancies of less than one week. The spatially averaged mean absolute difference (MAD) is 11.7 days across Eurasia and 15.1 days over North America. Mean biases (MB) are low across Eurasia (1.2 days) and North America (−3.1 days) regions. Larger discrepancies (MAD > 15 days) tend to occur

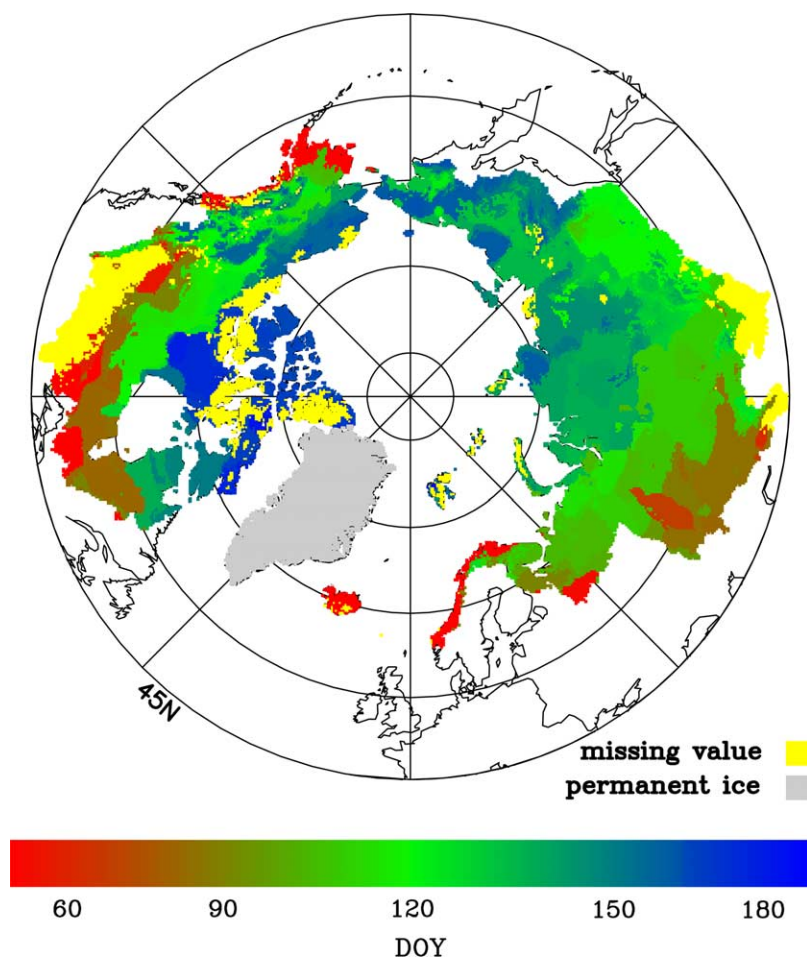


Fig. 6. Snow water initiation date ( $t_M$ ) for year 2000 from the pan-Arctic Water Balance Model (PWBM) (Rawlins et al., 2003). Gray shading masks regions of permanent ice and yellow shows grid cells where  $t_M$  is undefined, i.e. PWBM snow water is never  $>0$  mm for three consecutive days during spring 2000. Gray and yellow regions are excluded in our statistical analysis. These regions generally have low total 1999–2000 snowfall, additionally limiting both our analysis and the SeaWinds backscatter response.

in regions which experienced two or three distinct thaw events during spring of 2000. For example, the nature of large discrepancies can be illustrated by examining the scatterometer and hydrographic data across the Hanbury River basin in central Canada (Fig. 8). Although the algorithms for identifying  $t_P$  (Eq. (1)) and  $t_M$  both identify primary thaw near DOY 126, the scatterometer response in neighboring grid cells results in  $t_P$  (primary thaw) being defined as the second thaw event near DOY 141. Based on the observed discharge data, final snow ablation across the Hunbury basin and nearby regions may in fact occur shortly after DOY 150. The majority of large

discrepancies across the pan-Arctic arise under similar conditions; multiple thaw-freeze events are captured by the  $t_P$  (for one event) and  $t_M$  (a second event) algorithms. Nonetheless, approximately 60% of the discrepancies ( $t_M - t_P$  at each EASE-Grid) are between  $\pm 10$  days (Fig. 9). Over 15% of the pan-Arctic annual runoff occurs at grids with discrepancies in excess of  $-15$  days (primarily coastal regions). This leads to approximately 60% of the annual runoff occurring at grids cells with discrepancies between  $-22$  and  $10$  days. Thus, the wet coastal locations tend to decrease the correspondence (i.e. spatial statistics) between

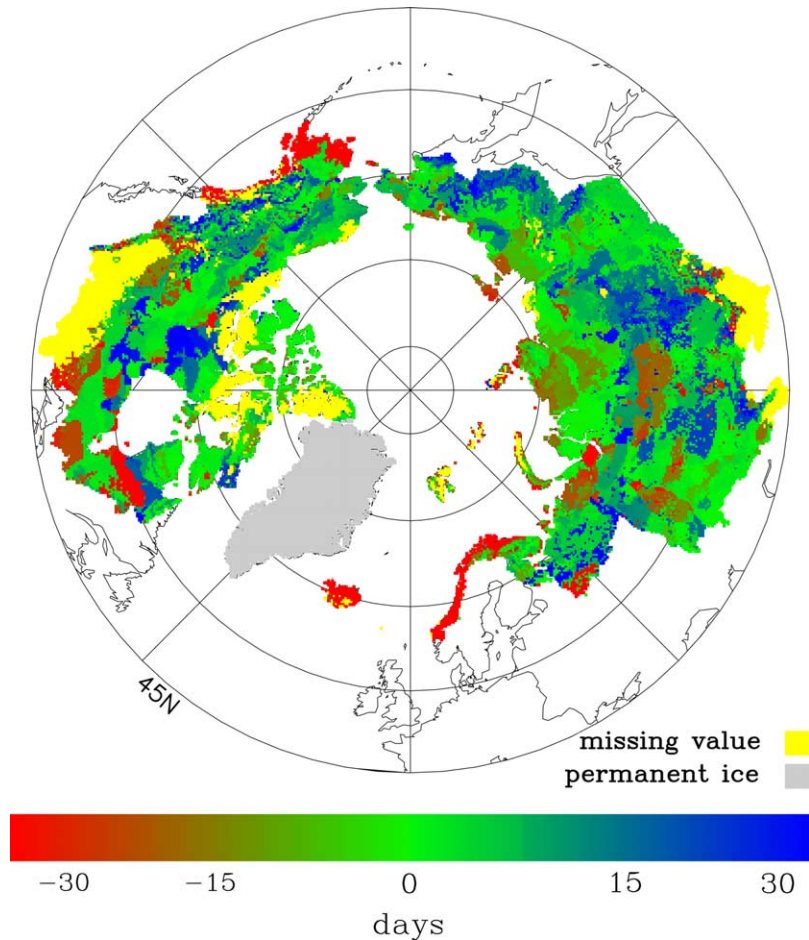


Fig. 7. Difference between PWBM snow water initiation date ( $t_M$ ) and scatterometer derived primary thaw date ( $t_P$ ) for 2000 across the pan-Arctic drainage basin. Gray and yellow grids are excluded from statistical analysis (see Fig. 6). Areas with large ( $MAD > 15$  days) differences are characterized by several thaw events throughout spring, and are largely due to identification of two thaw events ( $t_M$  for one event,  $t_P$  for another) separated by 2–3 weeks.

PWBM snow thaw- and scatterometer-derived estimates of pan-Arctic snow thaw timing. Grid cells encompassing over half of the 21 million  $\text{km}^2$  area analyzed have discrepancies of less than 1 week (inset of Fig. 9).

Landcover effects on the backscatter signal can be explored by defining a signal-to-noise value ( $R$ , unitless). We use the maximum decrease in daily backscatter from the 5-day mean (used to obtain  $t_P$ , Eq. (1)) for signal, with noise defined as the average absolute deviation of daily backscatter (December 1999–February 2000) from the backscatter running 5-day mean. Areas with stable snow cover seen by

repeated instrument scans are expected to have low backscatter variability during Dec–Feb (see Fig. 3a). Values of  $R$  are strongly correlated with tree cover, seasonal snowfall, and topographic complexity across the pan-Arctic, excluding Greenland. Across relatively flat regions (Fig. 10a), the largest  $R$  values occur with low tree cover and moderate-high snowfall. Strong correlations are also noted for moderately complex topography (Fig. 10b). Regions with the highest topographic complexity generally have low  $R$  values for all tree cover/snowfall classes (Fig. 10c). High snowfall in this group occur in grid cells across southeast Alaska, a region dominated by

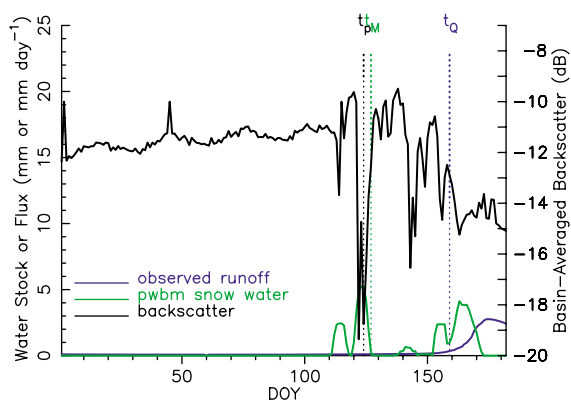


Fig. 8. Observed basin-average runoff, model snow water content, and daily SeaWinds backscatter for the Hanbury basin. This area experienced significant thawing near DOY 126 and 141, with a final basin thaw close to DOY 155. Large ( $>5$  dB) increases in the backscatter signal and coincident decreases in PWBM snow water suggest late spring refreeze of the landscape. Although  $t_M$  and  $t_P$  are nearly coincident, the backscatter time series in nearby areas results in  $t_P$  being defined for the thaw event at DOY 141, while  $t_M$  is determined as the earlier (DOY 126) event.

a highly variable maritime polar climate and high topographic complexity. Grid cells for Alaska in this group (snowfall  $>1000$  mm) do not drain directly to the Arctic Ocean. Wet winter storms along with frequent thaw events cause relatively high backscatter variability during winter and spring, leading to lower

$R$  values. For southeastern Alaska and similar regions, variable snow cover across opposing slopes, the presence of permanent ice and glaciers, and a highly dynamic, maritime winter/spring precipitation regime adversely affect our ability to extract a single, consistent radar backscatter spring thaw response.

## 5. Summary and conclusions

Approaches to estimating spring snow thaw at regional and continental scales are usually dependent on meteorological data (air temperature, precipitation, radiation) from a network of stations which, one assumes, can resolve the complex spatial variations in thaw. Across the pan-Arctic drainage basin, meteorological station density is sparse, which introduces a degree of uncertainty in thaw estimates. Timing of spring snow thaw inferred from the the SeaWinds scatterometer was compared to timing from two hydrological measures at 52 basins ( $5000\text{--}10,000$  km<sup>2</sup>) in Canada and Alaska to evaluate the correspondence between timing estimates from the remotely sensed, observed, and modeled data.

Agreement between timing of discharge increase ( $t_Q$ ) and scatterometer-derived thaw date ( $t_P$ ), determined as mean absolute deviation (MAD), averages

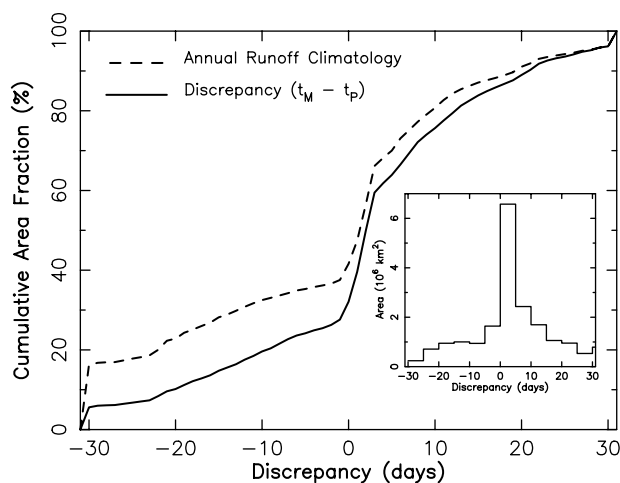


Fig. 9. Cumulative area histograms for  $t_M - t_P$  discrepancies (solid line) and annual runoff climatology (dashed line). Annual runoff climatology is taken from the pan-Arctic Water Balance Model annual runoff for the period 1980–2001. Curves are generated by summing the area for ordered discrepancies from least to greatest across all 32,896 analyzed grid cells (Fig. 7). Histogram of total area for discrepancies is shown in inset. Approximately 60% of the discrepancies are between  $\pm 10$  days, and over half of the area analyzed has an associated discrepancy of less than 1 week.

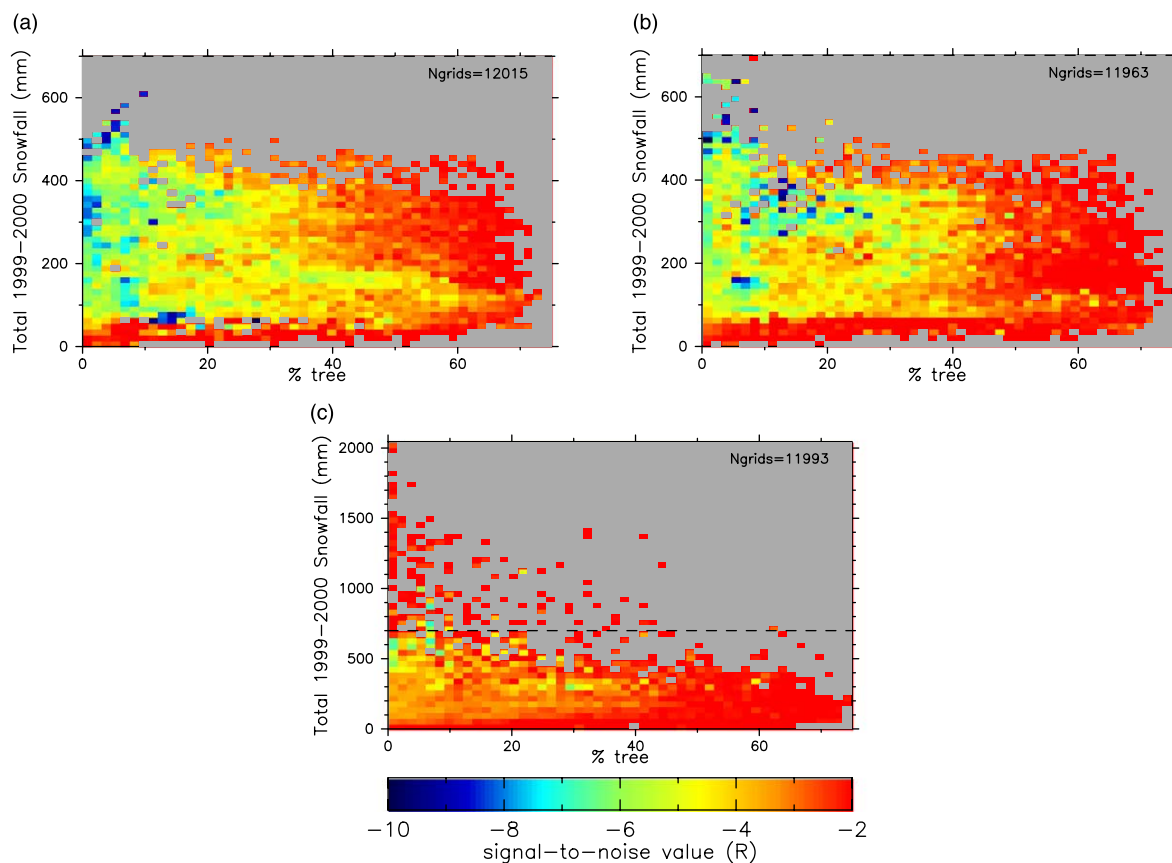


Fig. 10. Average signal to noise value ( $R$ ) grouped by percent tree cover and total 1999–2000 winter snowfall for (a) low (elevation standard deviation  $\leq 14.8$  m), (b) moderate ( $14.8 \text{ m} < \text{elevation standard deviation} \leq 52.2$  m), and (c) high (elevation standard deviation  $> 52.2$  m) topographic complexity.  $R = \delta_{\max} - \sigma_{\text{DJF}}$ , where  $\delta_{\max}$  is the maximum daily backscatter departure from previous 5-day backscatter average (Eq. (1)) and  $\sigma_{\text{DJF}}$  is the average absolute deviation of daily backscatter (December 1999–February 2000) from the running 5-day mean. Lower (more negative)  $R$  values indicate stronger signal relative to instrument seasonal noise. Instrument noise is low ( $< 0.25$  dB). The ‘noise’ we detect is the surface backscatter variability during winter. Plotted values are the average of all data in the two-dimensional tree cover/snowfall bin. The horizontal dotted line in (c) represents the extent of ordinate in (a) and (b).

21.5 days ( $r=0.45$ ). The mean bias  $MB$  is 6.1 days. The  $MAD$  is not unexpected given delays in snow thaw reaching stream systems which are known to occur, but difficult to model. Future studies which use field snow thaw snow water equivalent and snow thaw timing information will be useful in further evaluating the discrepancies presented here. The  $MAD$  between PWBM snow water initiation ( $t_M$ ) and  $t_P$  are lower (14.1 days,  $r=0.75$ ), since  $t_M$  and  $t_P$  are identifying the same process (snow thaw) which should precede the spring increase in discharge. Both comparisons show good correlations for basins with moderate to high runoff attributed to snow thaw. Individual

discrepancies tend to be higher for more heavily forested watersheds (tree cover  $> 50\%$ ) and the dry prairie basins. The correspondence between  $t_Q$  and  $t_P$  (and  $t_M$ ,  $t_P$ ) is best for high latitude basins. A critical component of our comparisons using  $t_Q$  involves the assumed presence of a measured hydrographic response to snow thaw. The analysis here included several watersheds with low snow amounts and small discharge increases in spring. These relatively low river flows introduce a degree of error in our identification of discharge increase. Moreover, in many areas, particularly along warmer southerly margins and maritime regions of the pan-Arctic, our

assumption of a single major snow thaw and discharge event in spring may not be valid. These areas tend to exhibit frequent snow thaw and discharge responses during winter and early spring from periodic warming events. The timing of  $t_Q$  and  $t_P$  across many regions suggest lags in the discharge increase following snow thaw, with shorter delays in high-latitude basins and longer lags to the south. Lags in the discharge response to snow thaw are expected due to known delays such as snow damming and lags in ground-water transport. Lags in timing are also related to differences in the infiltration capacity of permafrost and seasonally frozen soils. Future studies in specific moderate-sized watersheds involving scatterometer-derived timing of snow thaw could be useful in understanding the spatial pattern of lags between snow thaw and hydrological response as well as the factors contributing to the delays in snow thaw reaching Arctic river systems.

Good agreement between  $t_M$  and  $t_P$  across the 52 North American basins provide the motivation for expanding our analysis to the entire pan-Arctic drainage basin. Of the 32,896 analyzed grid cells almost half (49.4%) have  $t_M - t_P$  discrepancies of less than 1 week. Correspondence is slightly better across the Eurasia ( $MAD = 11.7$  days) as opposed to North America (15.1 days). Biases across both Eurasia and North America are low; 1.2 and  $-3.1$  days, respectively. Agreement between  $t_M$  and  $t_P$  is generally higher across tundra regions and lower along coastal margins. Larger discrepancies are primarily due to the identification of two separate thaw events by the  $t_M$  and  $t_P$  algorithms. That is, regions with higher discrepancies tend to be characterized by multiple thaw events through spring of 2000 and our algorithms selected different events. A majority of the  $t_M - t_P$  discrepancies are within  $\pm 10$  days.

Although signal-to-noise values are highest for regions of low tree cover, low topographic complexity, and high winter snowfall, the spatial pattern of discrepancies in timing is influenced by climatic type (e.g. the presence of multiple spring freeze/thaw cycles) as well as landscape factors. Our analysis shows that the best correspondence occurs at high latitude interior basins, areas that are most lacking in meteorological observation stations. Results of this study suggest that the SeaWinds backscatter is correlated with observed discharge (given lags

between snow thaw and hydrographic response) and model simulated snow thaw. Further studies are needed to determine if active radar instruments will be more useful for estimating spatial patterns of thaw than a absolute data of thaw. Research focusing on the influence of geophysical factors on radar response are also warranted. Although not studied here, future studies examining thaw timing from passive microwave time series may prove useful for trend analysis of pan-Arctic snow thaw timing.

### Acknowledgements

The authors gratefully acknowledge Charles Thompson (JPL) and Jason Lee (Caltech) for their assistance with processing the QuikSCAT data. QuikSCAT data were obtained from the JPL Physical Oceanography DAAC through the NASA Ocean Vector Wind Science Team. Alexander Shiklomanov (UNH/AARI) is acknowledged for frequent discussions regarding the river discharge data. We also thank Stanley Glidden (UNH) and Erika Podest (JPL) for their programming assistance. This research was supported by the NSF ARCSS program and NSF grants OPP-9910264, OPP-0230243, OPP-0094532, and NASA grant NAG5-9617. This work was performed at the University of New Hampshire's Water Systems Analysis Group and at the Jet Propulsion Laboratory, California Institute of Technology under contract to the National Aeronautics and Space Administration.

### References

- Brodzik, M.J., Knowles, K., 2002. EASE-Grid: a versatile set of equal-area projections and grids. In: Goodchild, M. (Ed.), *Discrete Global Grids*. National Center for Geographic Information and Analysis, Santa Barbara, CA, USA.
- Brown, J., Jr., Heginbottom, J.A., Melnikov, E.S., 1998. Circum-Arctic map of permafrost and ground-ice conditions. Technical Report, National Snow and Ice Data Center/World Data Center for Glaciology. Digital Media.
- Chapman, W.L., Walsh, J.E., 1993. Recent variations of sea ice and air temperature in high latitudes. *Bulletin of the American Meteorological Society* 74 (1), 33–47.
- Elachi, C., 1987. *Introduction to the Physics and Techniques of Remote Sensing*. Wiley, New York.

- Food and Agriculture Organization/UNESCO, 1995. Digital Soil Map of the World and Derived Properties, version 3.5, November, 1995. Original scale 1:5,000,000, UNESCO, Paris, France.
- Gesch, D.L., Verdin, K.L., Greenlee, S.K., 1999. New land surface digital elevation model covers the Earth. *AGU EOS Transactions* 80 (6), 69–70.
- Global Soil Data Task, 2000. Global gridded surfaces of selected soil characteristics (IGBP-DIS). Available from the ORNL Distributed Active Archive Center, Oak Ridge National Laboratory, Oak Ridge, Tennessee, USA.
- Hansen, M., DeFries, R., Townshend, J., Carroll, M., Dimiceli, C., Sohlberg, R., 2005. Global percent tree cover at a spatial resolution of 500 meters: first results of the MODIS vegetation continuous fields algorithm. *Earth Interactions* 7(10), 1–15.
- Hillard, U., Sridhar, V., Lettenmaier, D.P., McDonald, K.C., 2003. Assessing snowmelt dynamics with NASA scatterometer (NSCAT) data and a hydrologic process model. *Remote Sensing of Environment* 86, 52–69.
- Hinzman, L.D., Kane, D.L., 1991. Snow hydrology of a headwater Arctic basin 2. Conceptual analysis and computer modeling. *Water Resources Research* 27 (6), 1111–1121.
- Kalnay, E., Kanamitsu, M., Kistler, R., Collins, W., Deaven, D., Gandin, L., Iredell, M., Saha, S., White, G., Woolen, J., Zhu, Y., Chelliah, M., Ebisuzaki, W., Higgins, W., Janowiak, J., Ropelewski, K.C., Wang, J., Leetma, A., Reynolds, R., Jenne, R., Joseph, D., 1996. The NCEP/NCAR40-year reanalysis project. *Bulletin of the American Meteorological Society* 77, 437–471.
- Kane, D.L., 1997. Global Change and Arctic Terrestrial Ecosystems. *Ecol. Stud., The Impact of Arctic Hydrologic Perturbations on Arctic Ecosystems Induced by Climate Change*, vol. 124. Springer-Verlag, New York pp. 63–81.
- Kimball, J.S., McDonald, K.C., Frolking, S., Running, S.W., 2004a. Radar remote sensing of the spring thaw transition across a boreal landscape. *Remote Sensing of Environment* 89, 163–175.
- Kimball, J.S., McDonald, K.C., Frolking, S., Running, S.W., 2004b. Satellite radar remote sensing of seasonal growing seasons for boreal and subalpine evergreen forests. *Remote Sensing of Environment* 90, 243–258.
- King, M.D., Greenstone, R., 1999. Eos reference handbook: a guide to NASA's earth science enterprise and the earth observing system. In: King, M.D., Greenstone, R. (Eds.), Technical report NASA document NP-1999-08-134-GSFC, p. 361.
- Kraszewski, A., 1996. *Microwave Aquametry: Electromagnetic Wave Interaction with Water-Containing Materials*. IEEE Press, 484 pp.
- Lammers, R.B., Shiklomanov, A.I., Vörösmarty, C.J., Fekete, B.M., Peterson, B.J., 2001. Assessment of contemporary Arctic river runoff based on observational discharge records. *Journal of Geophysical Research* 106 (D4), 3321–3334.
- Liang, X., Lettenmaier, D.P., Wood, E.F., Burges, S.J., 1994. A simple hydrologically based model of land surface water and energy fluxes for general circulation models. *Journal of Geophysical Research* 99, 14415–14428.
- McDonald, K.C., Kimball, J.S., Njoku, E., Zimmermann, R., Zhao, M., 2004. Variability in springtime thaw in the terrestrial high latitudes: Monitoring a major control on the biospheric assimilation of atmospheric CO<sub>2</sub> with spaceborne microwave remote sensing. *Earth Interactions* 8, 1–23.
- Nghiem, S.V., Tsai, W.Y., 2001. Global snow cover monitoring with spaceborne K<sub>u</sub>-band scatterometer. *IEEE Transactions on Geoscience and Remote Sensing* 39, 2118–2134.
- NOAA/NESDIS, 1999. Northern hemisphere snow cover data, operational 89×89 northern hemisphere snow cover data 1973-present. Technical Report.
- NSIDC, 1995. The Equal-Area Scalable Grid. Technical report, National Snow and Ice Data Center. <http://nsidc.org/data/ease/index.html>
- Osterkamp, T.E., Romanovsky, V.E., 1999. Evidence for warming and thawing of discontinuous permafrost in Alaska. *Permafrost and Periglacial Processes* 10 (1), 17–37.
- Parish, D.F., Derber, J.C., 1992. The national meteorological center's spectral statistical interpolation analysis system. *Monthly Weather Review* 120, 1747–1763.
- Peterson, B.J., Holmes, R.M., McClelland, J.W., Vörösmarty, C.J., Lammers, R.B., Shiklomanov, A.I., Shiklomanov, I.A., Rahmstorf, S., 2002. Increasing river discharge to the Arctic ocean. *Science* 298, 2171–2173.
- Raney, K.R., 1998. In: Henderson, F.M., Lewis, A.J. (Eds.), *Radar Fundamentals: Technical Perspective, of Principles and Applications of Imaging Radar*, vol. 2. Wiley, New York.
- Rawlins, M.A., Willmott, C.J., 2003. Winter air-temperature change across the terrestrial arctic, 1961–1990. *Arctic, Antarctic and Alpine Research* 35 (4), 530–537.
- Rawlins, M.A., Lammers, R.B., Frolking, S., Fekete, B.M., Vörösmarty, C.J., 2003. Simulating pan-Arctic runoff with a macro-scale terrestrial water balance model. *Hydrological Processes* 17, 2521–2539.
- Robeson, S.M., 2004. Trends in time-varying percentiles of daily minimum and maximum air temperature over North America. *Geophysical Research Letters* 31, 101029/2003GL019019.
- Romanovsky, V., Burgess, M., Smith, S., Yoshikawa, K., Brown, J., 2002. Permafrost temperature records: indicators of climate change. *EOS AGU Transactions* 83 (50), 589–594.
- Rothrock, D.A., Zhang, J., Yu, Y., 2003. The arctic ice thickness anomaly of the 1990s: a consistent view from observations and models. *Journal of Geophysical Research* 108 (C3), 3083. doi:10.1029/2001JC001208.
- Serreze, M.C., Walsh, J.E., Chapin III, F.S., Osterkamp, T., Dyurgerov, M., Romanovsky, V., Oechel, W.C., Morison, J., Zhang, T., Barry, R., 2000. Observation evidence of recent change in the northern high-latitude environment. *Climate Change* 46, 159–207.
- Serreze, M.C., Maslanik, J.A., Scambos, T.A., Fetterer, F., Stroeve, J., 2002. A record minimum sea ice cover in the Arctic Ocean for summer. *Geophysical Research Letters* 30, 110. doi:10.1029/2002GL016406.
- Serreze, M.C., Clark, M.P., Bromwich, D.H., 2003. Monitoring precipitation over the Arctic terrestrial drainage system: data requirements, shortcomings, and applications of atmospheric reanalysis. *Journal of Hydrometeorology* 4 (2), 387–407.

- Shi, J., Dozier, J., 1995. Inferring snow wetness using c-band data from SIR-C's polarimetric synthetic aperture radar. *IEEE Transactions on Geoscience and Remote Sensing* 34 (4), 905–914.
- Shiklomanov, I.A., Shiklomanov, A.I., Lammers, R.B., Peterson, B.J., Vörösmarty, C.J., 2000. The dynamics of river water inflow to the Arctic Ocean. In: Lewis, E.I. et al. (Ed.), *The Freshwater Budget of the Arctic Ocean*. Kluwer, Dordrecht, pp. 281–296.
- Shiklomanov, A.I., Lammers, R.B., Vörösmarty, C.J., 2002. Widespread decline in hydrological monitoring threatens Pan-Arctic research. *EOS Transactions, American Geophysical Union* 83 (2), 13–17.
- Sturm, M.J., Holmgren, J., Liston, G.E., 1995. A seasonal snow cover classification system for local to global applications. *Journal of Climate* 8 (5), 1261–1283.
- Ulaby, F.T., Dobson, M.C., 1986. *Handbook of Radar Scattering Statistics for Terrain*, vol. 3. Artec House, Dedham, MA.
- Ulaby, F.T., Moore, R.K., Fung, A.K., 1989. *Microwave Remote Sensing-Active and Passive*. Artec House, Dedham, MA.
- Uppala, S., Gibson, J.K., Fiorino, M., Hernandez, A., Kallberg, P., Li, X., Onogi, K., Saarinen, S., 2000. ECMWF Second Generation Reanalysis. In *Proceedings of the Second WCRP International Conference on Reanalysis*, pp. 9–13. WMO/TD-No. 985.
- USGS EROS Data Center, 1996. Global 30 arc second elevation data set GTOPO30. <http://edcwww.cr.usgs.gov/landdaac/gtopo30/README.html>
- Vörösmarty, C.J., Moore III, B., Grace, A.L., Gildea, M.P., Melillo, J.M., Peterson, B.J., Rastetter, E.B., Steudler, P.A., 1989. Continental scale models of water balance and fluvial transport: an application to South America. *Global Biogeochemical Cycles* 3 (3), 241–265.
- Vörösmarty, C.J., Hinzman, L.D., Peterson, B.J., Bromwich, D.H., Hamilton, L.C., Morrison, J., Romanovsky, V.E., Sturm, M., Webb, R.S., 2001. The hydrologic cycle and its role in arctic and global environmental change: a rationale and strategy for synthesis study, Technical report. Arctic Research Consortium of the U.S., Fairbanks, AK.
- Waring, R.H., Way, J.B., Hunt, E.R., Morrissey, L., Ranson, K.J., Weishampel, J.F., Oren, R., Franklin, S.E., 1995. Imaging radar for ecosystem studies. *Bioscience* 45 (10), 715–723.
- Willmott, C.J., Rowe, C.J., Mintz, Y., 1985. Climatology of the terrestrial seasonal water cycle. *Journal of Climate* 5, 589–606.
- Winebrenner, D.P., Nelson, E.D., Colony, R., West, R., 1994. Observation of melt onset on multiyear Arctic sea ice using the ERS-1 synthetic aperture radar. *Journal of Geophysical Research* 99, 22425–22441.
- Wismann, V., 2000a. Monitoring of seasonal thawing in Siberia with ERS scatterometer data. *IEEE Transactions on Geoscience and Remote Sensing* 38, 1804–1809.
- Wismann, V., 2000b. Monitoring of seasonal thawing on Greenland with ERS scatterometer data. *IEEE Transactions on Geoscience and Remote Sensing* 38, 1821–1826.